IEEE TRANSACTIONS ON MAGNETICS

## Torque Analysis in Coaxial Magnetic Gears Considering Nonlinear Magnetic Properties and Spatial Harmonics

Zhangxian Deng<sup>®</sup>, Ismail Nas<sup>®</sup>, and Marcelo J. Dapino<sup>®</sup>

NSF IUCRC Smart Vehicle Concepts Center, Department of Mechanical and Aerospace Engineering, The Ohio State University, Columbus, OH 43210 USA

A coaxial magnetic gear (CMG) consisting of an inner ring, outer ring, and flux modulator exhibits relatively large torque density at low operating cost and low noise level. To guide the selection of soft magnetic materials for the flux modulator, this paper first incorporates the Jiles-Atherton model within a finite-element (FE) framework. The influence of nonlinear magnetic properties on end-effect losses (magnetic flux leakage and fringing) is then investigated with the objective of maximizing the pullout torque. For flux modulators whose initial magnetic permeability and saturation flux density exceed certain threshold value, the pullout torque of a CMG becomes insensitive to magnetic properties and end-effect losses can be efficiently calculated from a 2-D FE model together with a constant torque reduction ratio. This paper presents a systematic torque surface method that can decouple the analysis of average torque and torque ripples. This method has been implemented to evaluate load dependence and rotation speed fluctuation of a CMG.

Index Terms—Coaxial magnetic gear (CMG), end effect, finite-element (FE) modeling, flux modulation, torque surface method.

#### I. INTRODUCTION

AGNETIC gears (MGs) that transmit torque and motion via magnetic coupling can provide low maintenance cost and low noise to electrical drives. Compared with mechanical gears, MGs offer a simpler design, in that they do not require seals or lubrication, and tolerate high temperatures considering the Curie temperature of NdFeB magnets exceed 300°C whereas common lubricants start degrading above 100°C. The torsional stiffness of MGs is relatively small and thus they require no overload protection mechanisms or clutches. Due to the absence of mechanical contact, MGs exhibit no backlash. Early studies have demonstrated magnetic spur gears in which conventional gear teeth were replaced with permanent magnets (PMs) [1], [2]. However, these configurations exhibit extremely low torque density, which is defined as the ratio of transmitted torque to the volume of MG. With the advent of rare-earth magnets and superconducting materials, MGs have become feasible. Cycloid [3], harmonic [4], and worm [5], [6] MGs have been discussed in the literature.

The coaxial MG (CMG) configuration currently provides the maximum torque density along with reasonably large gear ratios (up to 21:1). This configuration was presented by Martin [7], but it was Atallah and Howe [8] who first demonstrated a large torque density that is comparable to conventional planetary gears (50–150 kN·m/m³) [9], [10]. As shown in Fig. 1, a typical CMG consists of an inner ring with  $p_{\rm in}$  magnet pole pairs, an outer ring with  $p_{\rm out}$  magnet pole pairs, and a magnetic flux modulator with  $p_{\rm mod}$  pole pieces. The magnetic coupling with a negative gear ratio is achieved by selecting  $p_{\rm mod} = p_{\rm in} + p_{\rm out}$ . The inner ring is connected

Manuscript received May 22, 2018; revised August 11, 2018 and November 4, 2018; accepted November 29, 2018. Corresponding author: M. J. Dapino (e-mail: dapino.1@osu.edu).

Color versions of one or more of the figures in this paper are available online at http://ieeexplore.ieee.org.

Digital Object Identifier 10.1109/TMAG.2018.2885729

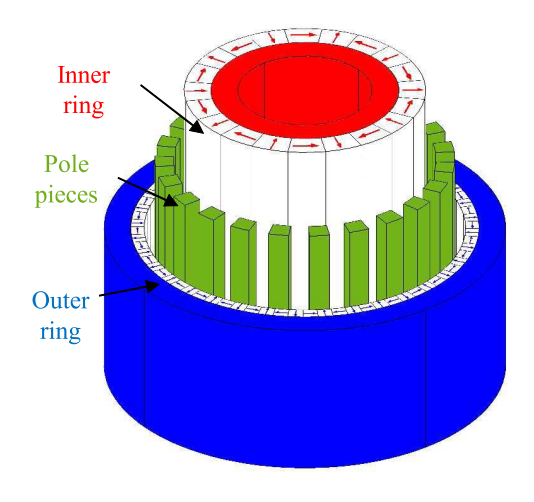


Fig. 1. Exploded view of a CMG. Arrows: magnetization directions of PMs.

to a high-speed input shaft. The low-speed output shaft can be connected to the flux modulator or the outer ring. In this paper, the flux modulator is stationary and the outer ring is selected as the output end. Thus, the corresponding gear ratio is  $G_r = -p_{\text{out}}/p_{\text{in}}$ . To reduce the overall device size, torque ripples, and undesirable radial forces, variations of the CMG configuration have been proposed, including flux switching MG [13] and skewed CMG [14]. Similarly, the concepts of CMG and electrical motors have been combined to create electromagnetic actuators such as pseudo-direct drives [11] and magnetic geared machines [12].

The development and optimization of a CMG rely on efficient and accurate models. Because of the similarity between CMGs and conventional PM motors, CMGs have been modeled analytically following the concepts of conformal transform [15] and summation of modes [16].

These analytical models [17], [18] are computationally efficient, especially when evaluating cogging torque or torque ripples [19]. However, they are constructed based on several strong assumptions, including infinite magnetic permeability of the modulator pole pieces, no flux leakage along the axial direction (end-effect losses), and no hysteresis losses. Furthermore, existing analytical models are inadequate for CMGs whose pole pieces have irregular shapes. The load dynamics including rotation speed fluctuation and the slipping effect are excluded, since the gear ratio is enforced by assigning constant speeds to both rings as boundary conditions.

Lumped parameter models, or reluctance network models, have been developed by discretizing the entire CMG system into small elements [20], [21]. In each element, the magnetic material is modeled as a linear reluctance and the PM is modeled as a magnetomotive force (MMF) source. Most of the assumptions associated with the analytical models have been lifted in lumped parameter models. For instance, end-effect losses have been described by modifying the magnetic reluctance along the axial direction; the nonlinear magnetic permeability of the flux modulator can be defined via piecewise linear functions; and the load dynamics can be described by Newton's law [20], [21]. Refining the discretization quality leads to higher model accuracy but at the expense of increased computational time [22]. Hence, prior empirical knowledge of the CMG system is required to balance model accuracy and efficiency.

The magnetic coupling in the CMG system can be described by Maxwell's equations. Analytical solutions of Maxwell's equations have been derived based on Poisson's equations and Laplace's equations [23], [24]. However, these analytical solutions require a large number of empirical parameters and are computationally intensive. Maxwell's equations can also be solved by finite-element (FE) analysis. Rasmussen et al. [25] first developed a 2-D FE model to calculate the maximum output torque (pullout torque) of a CMG. Jian et al. [26] later implemented 2-D FE models to investigate the influence of magnet pole pairs on the higher harmonics in the output torque (torque ripples). Although 2-D FE models are efficient, they overestimate the pullout torque because they neglect end-effect losses. Jungmayr et al. [14] recently developed a 3-D FE model that considers end-effect losses to quantify the radial force and torque ripples. Gerber et al. [27] studied the influence of geometric parameters on end-effect losses by comparing 2-D and 3-D FE modeling results. Li et al. [28] described and quantified the effect of hysteresis on torque capacity, whereas Filippini et al. [29] implemented a hysteresis model for iron poles in a 2-D FE construct to include eddy currents and hysteresis losses. Efficient FE methods considering material nonlinearity and load dynamics are currently limited.

This paper investigates the influence of the nonlinear magnetic properties on the pullout torque and end-effect losses using FE analysis. The coupling between the nonlinear material properties as described by the Jiles-Atherton (JA) model and the FE framework is detailed in Section II. The pullout torque is quantified with respect to initial magnetic permeability and saturation flux density in Section III. The flux

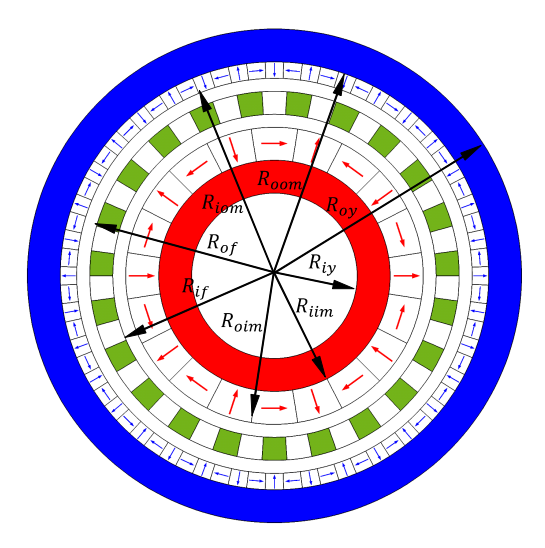


Fig. 2. Cross-section view of the CMG design considered in this paper.

# TABLE I DIMENSIONS OF THE CMG

Design parameter	Value
$p_{in}$	4
$p_{out}$	13
$p_{mod}$	17
Axial thickness $L$ [mm]	25.4
$R_{oy}$ [mm]	71.12
$R_{oom}$ [mm]	64.77
$R_{iom}$ [mm]	58.42
$R_{of}$ [mm]	55.54
$R_{if}$ [mm]	49.95
$R_{oim}$ [mm]	47.83
$R_{iim}$ [mm]	35.13
$R_{iy}$ [mm]	22.43
Remanence of magnets $B_{rem}$ [T]	1.465

leakage mechanisms and end-effect losses are evaluated by comparing 2-D and 3-D FE results in Section IV. Finally, in Section V, this paper decouples the torque ripples and the average torque in CMG and presents a systematic design strategy to investigate the load dynamics.

# II. NONLINEAR MAGNETIC PROPERTIES IN FE FRAMEWORK

## A. CMG Configuration

Fig. 2 presents the cross section of a CMG whose dimensions and material properties are listed in Table I. On each ring, a series of magnetic poles forms a Halbach array and each magnet pole consists of four PMs. The total number of magnetic poles on the outer ring is  $p_{\text{out}} = 13$ ; the total magnetic poles on the inner ring is  $p_{\text{in}} = 4$ . The flux modulator is fabricated by alternating  $p_{\text{mod}} = 17$  soft magnetic pole pieces and 17 air gaps. The size of the pole pieces is the same as that of the air gaps. In this paper, the flux modulator is fixed and the outer ring is connected to the low-speed shaft. Hence, the gear ratio is  $G_r = -13/4$ . All the PMs are supported by yokes that are made of soft magnetic materials. The magnetic flux leaking through the yokes is relatively small and has negligible influence on the coupling torque. Moreover,

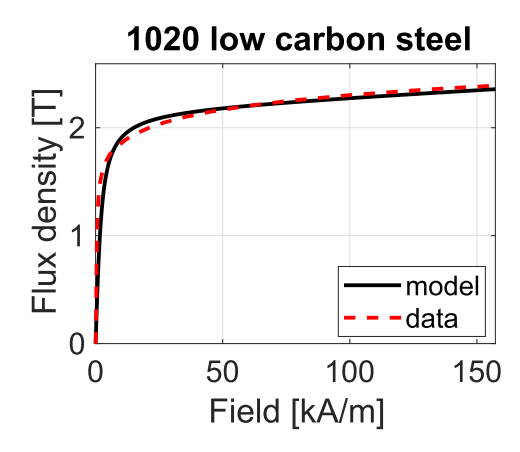


Fig. 3. Comparison of measured and approximated flux density versus magnetic field curves of AISI 1020 low carbon steel.

the yoke is much larger than the flux modulator which results in negligible magnetic reluctance. As a result, the relative magnetic permeability of both yokes can be approximated by a constant value of  $10^4$ .

## B. Parametrized Magnetic Properties

The soft magnetic flux modulator pole pieces exhibit nonlinear magnetic permeability and hysteresis loss that has been mathematically described by the JA model [30]. Ignoring the hysteresis loss, the nonlinear magnetic permeability, or nonlinear flux density versus field relationship, is described as

$$B = B_s \left( \coth \left( \frac{H_e}{a} \right) - \frac{a}{H_e} \right) + \mu_0 H \tag{1}$$

where B denotes the magnetic flux density, H denotes the magnetic field,  $B_s$  is the saturation flux density of the soft magnetic material,  $\mu_0$  is the magnetic permeability of vacuum, a is a smoothing factor controlling the initial permeability of the material, and the effective field is

$$H_e = H - \alpha \frac{B - \mu_0 H}{\mu_0}.\tag{2}$$

To reduce the total number of variables and simplify later discussion, this paper assumes  $\alpha = a\mu_0/B_s$ . Table II summarizes the JA model parameters for selected commercially available soft magnetic materials, where the initial relative magnetic permeability is calculated as

$$\mu_{r,\text{in}} = \frac{1}{\mu_0} \left. \frac{\partial B}{\partial H} \right|_{H=0}. \tag{3}$$

Anhysteretic flux density versus field curves of AISI 1020 low carbon steel, including both experimental and modeling results, are compared in Fig. 3. The rms error between the JA model and data from commercially available materials is listed in Table II. The close fit shows that the JA model is able to accurately describe the nonlinear magnetic properties.

TABLE II

JA MODEL PARAMETERS FOR SELECTED SOFT MAGNETIC

MATERIALS [31], [32]

Materials	$B_s$ [T]	a [A/m]	$\mu_{r,in}$ [-]	Error [%]
GO electrical steel	2.01	13	$6.14 \times 10^4$	7.7
NGO electrical steel	1.74	90	$7.67 \times 10^{3}$	5.1
AISI 1020	2.18	660	$1.31 \times 10^{3}$	4.8
AISI 416	1.60	730	$8.71 \times 10^{2}$	3.8
Iron powder core	0.42	9000	$1.96 \times 10^{1}$	0.6
Metglas 2605S3A	1.45	16	$3.60 \times 10^{4}$	1.8
Ferrite core	0.37	28	$5.22 \times 10^{3}$	5.1
Kool- $\mu$ powder core	1.05	15000	$2.88 \times 10^{1}$	1.7
Supermalloy	7.5	0.72	$3.89 \times 10^{6}$	2.2

#### III. MATERIAL SELECTION FOR FLUX MODULATOR

As shown in Fig. 2, when an outward PM on the inner ring, an outward PM on the outer ring, and the edge of a flux modulator pole piece are aligned, the output torque reaches a maximum, defined as the pullout torque. This paper conducts a parametric study and numerically compares the performance of the CMG in terms of the pullout torque for various soft magnetic materials. Computational work in this paper was performed on the Owens cluster at the Ohio Supercomputer Center [33]. The pullout torque  $T_{\text{out}}^{3-D}$  is calculated from a 3-D FE simulation. The value of  $B_s$  ranges from 0.2 to 2.6 T in 0.3 T increments; the value of a which determines the initial magnetic permeability is logarithmically distributed from  $10^1$  to  $10^{4.5}$  in nine steps. Thus, the corresponding  $\mu_{r,in}$ ranges from 2.51 to  $1.03 \times 10^5$ . To compare the modeling results with those presented in the literature, a normalized pullout torque  $E_m$  is defined as

$$E_m = \frac{T_{\text{out}}^{3-D}}{T_{\text{out}}^{\text{max}}}. (4)$$

Here,  $T_{\rm out}^{\rm max}$  is the pullout torque calculated from the 2-D FE model in which the pole pieces have a constant permeability of  $10^4$ . The value of  $T_{\rm out}^{\rm max}$  is the maximum possible output torque from the CMG, corresponding to the case when end-effect losses and the saturation of the pole pieces are ignored.

As shown in Fig. 4, the output torque increases monotonically with respect to  $\mu_{r,\rm in}$  and  $B_s$ . When  $B_s/B_{\rm rem}$  exceeds 106%, the normalized pullout torque  $E_m$  no longer increases with respect to  $B_s$ . A similar threshold value can be found for the initial magnetic permeability  $\mu_{r,\rm in}$ . When  $\mu_{r,\rm in} > 178$ , the pullout torque becomes insensitive to  $\mu_{r,\rm in}$ . According to Table II, AISI 1020 low carbon steel is one of the appropriate material options for the flux modulator pole pieces; as such, it will be utilized in all later discussion. Due to end-effect losses, the pullout torque can only reach 65% of the ultimate maximum  $T_{\rm out}^{\rm max}$  predicted by the 2-D simulation for the particular CMG configuration defined in Fig. 2 and Table I.

## IV. END-EFFECT LOSSES

Fig. 5 shows the four possible magnetic flux paths around the inner and outer rings when the CMG is at the pullout torque position. Paths 1 and 2 represent the magnetic flux sourced from the inner ring, modulated by the flux modulator,

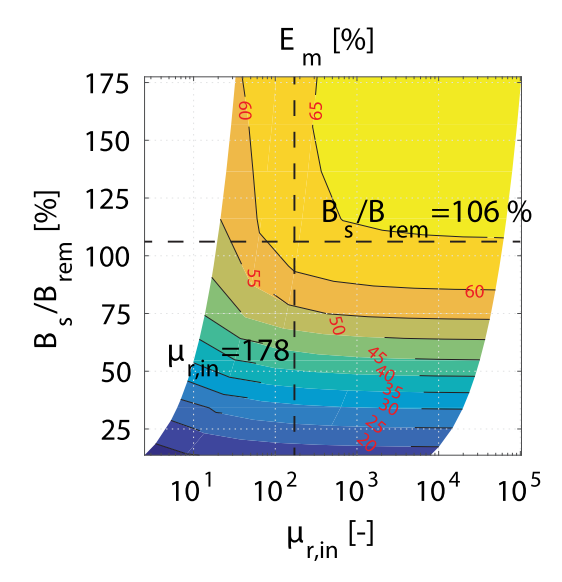


Fig. 4. Normalized pullout torque  $E_m$  versus the normalized saturation flux density  $B_s/B_{\rm rem}$  and initial permeability  $\mu_{r,{\rm in}}$ .

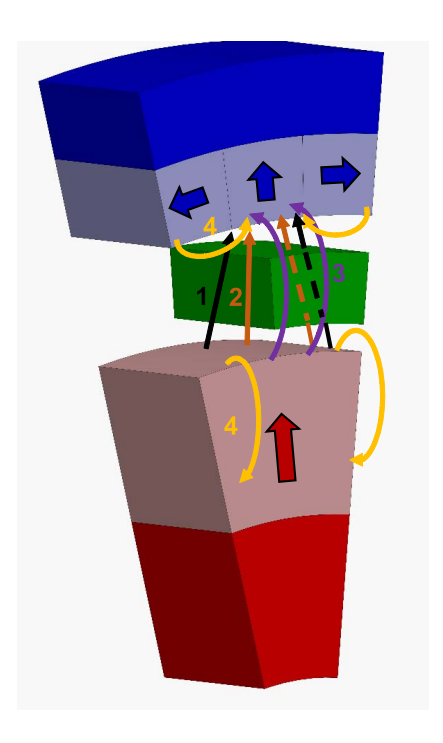


Fig. 5. Four possible magnetic flux paths between the inner and outer rotors. For paths 1 and 2, solid lines and dashed lines represent the coupled magnetic flux going through the air and the pole pieces, respectively.

and coupled with the outer ring. Part of this coupled magnetic flux, or path 1, leads to a desirable average torque. Due to the discontinuity in the flux modulator and the Halbach arrays, the rest of the coupled magnetic flux, as illustrated by path 2, does not contribute to the average torque but introduces torque ripples or disturbance forces. Path 3 demonstrates the magnetic flux flowing through the air around the CMG. This phenomenon, also known as fringing, is one source of end-effect losses. The other source of end-effect losses, or the leakage effect, is described by path 4 where the magnetic flux returns to its originating magnetic pole.

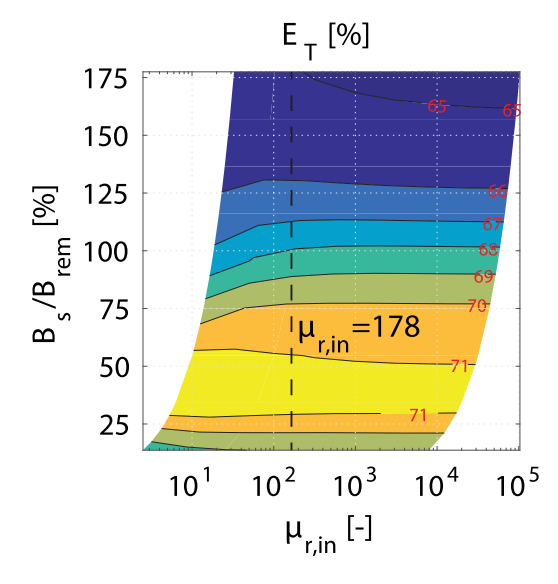


Fig. 6. Torque reduction ratio  $E_T$  versus the normalized saturation flux density  $B_S/B_{\rm rem}$  and initial permeability  $\mu_{r,\rm in}$ .

To reduce computational time, most of the existing numerical studies in the literature are based on 2-D FE models. However, 2-D FE models cannot describe paths 3 and 4. Thus, they overestimate the pullout torque. This paper quantifies end-effect losses by comparing the 2-D and 3-D FE results. End-effect losses are quantified by a torque reduction ratio

$$E_T = \frac{T_{\text{out}}^{3-D}}{T_{\text{out}}^{2-D}} \tag{5}$$

where  $T_{\text{out}}^{2-D}$  is the pullout torque calculated from a 2-D FE model with the same material properties.

Fig. 6 presents the values of  $E_T$  with respect to  $B_s/B_{\rm rem}$ and  $\mu_{r in}$ , where their ranges and step sizes are the same as those utilized in Section III. Overall, the variation in  $E_T$  is less than 1% within the range of  $\mu_{r,in}$  discussed in this paper. Specifically, when  $\mu_{r,in} > 178$ , which is the threshold value predicted in Section III, the initial magnetic permeability  $\mu_{r,in}$ has negligible influence on  $E_T$ . The value of  $E_T$  peaks when  $B_s/B_{\rm rem}$  is between 27% and 52%. The initial increment in  $E_T$ is due to the dominant effect of magnetic flux path 2 rather than a reduction in end-effect losses. For a small  $B_s/B_{\rm rem}$ ratio, the flux modulator pole pieces are easily saturated by the PMs. Once the flux modulator is saturated, path 2 becomes the preferable route for the coupled magnetic flux, which reduces  $T_{\text{out}}^{2-D}$  and results in a larger  $E_T$ . When both  $\mu_{r,\text{in}}$  and  $B_s$  of the selected soft magnetic materials exceed the threshold values presented in Section III, the value of  $E_T$  remains constant at 65%. This constant  $E_T$  together with an efficient 2-D FE model are able to accurately predict the pullout torque along with end-effect losses.

#### V. TORQUE SURFACE METHOD

## A. Torque Surface

For a given CMG, the torque coupling at any time t can be defined by the angular position of each component. In this

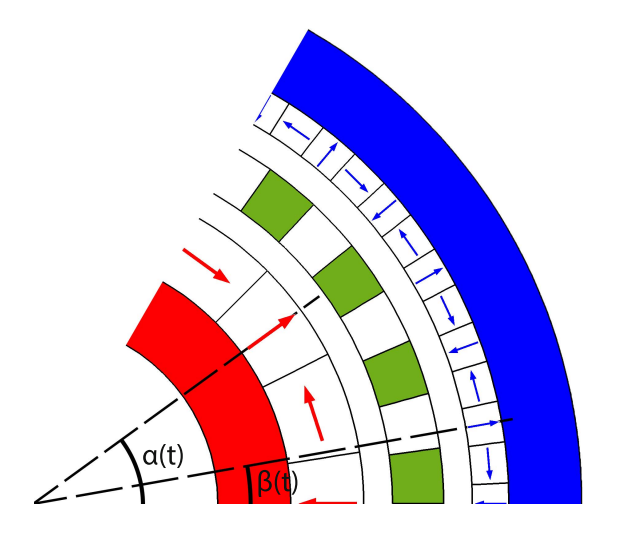


Fig. 7. Angular position of the inner rotor  $\alpha(t)$  and the outer rotor  $\beta(t)$ .

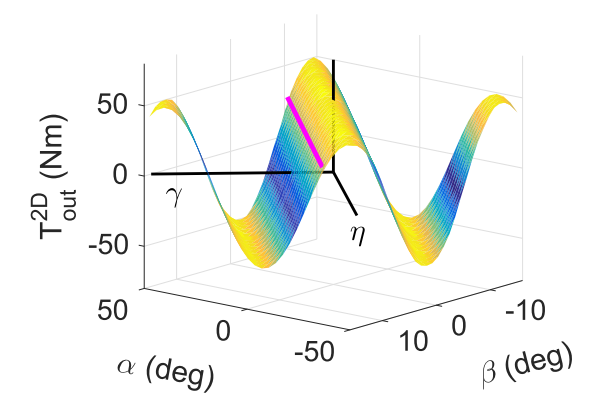


Fig. 8. Output torque represented in both  $\alpha-\beta$  and  $\gamma-\eta$  coordinate systems. Purple line: operational line of the CMG.

paper, the flux modulator is stationary. The angular position of the inner ring  $\alpha(t)$  and the angular position of the outer ring  $\beta(t)$  can uniquely determine the magnetic coupling in the CMG. As shown in Fig. 7,  $\alpha(t)$  is the angle between one of the outward PMs on the inner ring and the horizontal direction;  $\beta(t)$  is the angle between one of the outward PMs on the outer ring and the horizontal direction. The coupling torque reaches the maximum when  $\alpha(t) = \beta(t) = 0$ . This paper ignores eddy current losses and thus the time dependence in the angular positions can be ignored.

A 2-D FE model is constructed for the CMG dimensions and material properties presented in Table I. The flux modulator is made of laminated AISI 1020 low carbon steel such that ignoring eddy current losses is a valid assumption. Fig. 8 shows the modeling results of  $T_{\rm out}$  with respect to  $\alpha$  and  $\beta$ , where  $\alpha$  ranges from  $-\pi/p_{\rm in}$  to  $\pi/p_{\rm in}$  and  $\beta$  ranges from  $-\pi/p_{\rm out}$  to  $\pi/p_{\rm out}$ . Properties of this torque surface are analyzed in Sections V-B–V-E.

## B. Alternative $\gamma - \eta$ Coordinate System

The output torque  $T_{\text{out}}$  is calculated as the change of the magnetic energy W stored in the outer rotor with respect to

the angular position  $\beta$  such that [19]

$$T_{\text{out}}(\alpha, \beta) = -\frac{\partial W(\alpha, \beta)}{\partial \beta}$$
$$= -\frac{\partial}{\partial \beta} \left( \frac{1}{2\mu_0} \int_V |\vec{B}(\alpha, \beta)|^2 dV \right)$$
(6)

where  $\vec{B}(\alpha, \beta)$  denotes the magnetic flux density distribution. In order to calculate the output torque, we assume that the magnetic energy  $W(\alpha, \beta)$  is stored where the reluctance is largest, that is in the air gap between the outer ring and the flux modulator [19]. Hence

$$W(\alpha, \beta) = \frac{t_{\text{gap}}}{8\pi^2 \mu_0 r L} \int_0^{2\pi} |\vec{\phi}(\alpha, \beta, \theta)|^2 d\theta \tag{7}$$

where  $t_{\rm gap} = R_{\rm oom} - R_{\rm oim}$  is the radial thickness of the outer air gap, the air-gap location  $r = (R_{\rm of} + R_{\rm oim})/2$ , and  $\vec{\phi}(\alpha, \beta, \theta)$  is the magnetic flux at angle  $\theta$ .

The magnetic flux in the outer air gap has contributions from the outer ring and the inner ring. Application of the superposition principle gives [18]

$$|\vec{\phi}(\alpha, \beta, \theta)| = [F_{\text{in}}(\alpha, \theta) + F_{\text{out}}(\beta, \theta)]P(\theta). \tag{8}$$

Here,  $F_{\text{in}}(\alpha, \theta)$  and  $F_{\text{out}}(\beta, \theta)$  are the MMFs created by the inner and outer magnet rings, respectively, where

$$F_{\rm in}(\alpha, \theta) = \sum_{m=1,3...}^{\infty} a_m \sin[mp_{\rm in}(\theta + \alpha)]$$
 (9)

and

$$F_{\text{out}}(\beta, \theta) = \sum_{n=1,3...}^{\infty} a_n \sin[np_{\text{out}}(\theta + \beta)].$$
 (10)

The permeance of the flux modulator is

$$P(\theta) = a_{l0} + \sum_{l=1,3}^{\infty} a_l \sin(l p_{\text{mod}} \theta)$$
 (11)

where  $a_{l0}$ ,  $a_m$ ,  $a_n$ , and  $a_l$  are the Fourier series constants.

The aforementioned analytical model indicates that the output torque consists of the desirable average torque and undesirable higher harmonics (torque ripples). Fig. 8 suggests that the analysis of the average torque and the torque ripples can possibly be decoupled by choosing an alternative coordinate system,  $\gamma - \eta$ . The slope of the  $\eta$  axis in the  $\alpha - \beta$  coordinate system is  $-G_r$ . Hence, for any static loads, the CMG operates following the operational lines (one is illustrated by a purple line in Fig. 8) which are parallel to the  $\eta$  axis. The fluctuation in  $T_{\text{out}}$  when the CMG operates along the operational line is the torque ripple. The coordinate  $\eta$  is thus termed torque ripple argument. The  $\gamma$  axis, which is perpendicular to the  $\eta$  axis, indicates the changes in average torque as the initial positions  $\alpha$  and  $\beta$  vary. Hence, the coordinate  $\gamma$  is termed average torque argument. The expression of output torque  $T_{\text{out}}$ is converted into the  $\gamma - \eta$  coordinate system using the chain

$$T_{\text{out}} = -\frac{\partial W(\alpha, \beta)}{\partial \beta} = -\frac{\partial W(\gamma, \eta)}{\partial \gamma} \frac{\partial \gamma}{\partial \beta} - \frac{\partial W(\gamma, \eta)}{\partial \eta} \frac{\partial \eta}{\partial \beta}$$
$$= -p_{\text{out}} \frac{\partial W(\gamma, \eta)}{\partial \gamma} - p_{\text{in}} \frac{\partial W(\gamma, \eta)}{\partial \eta}$$
$$= -p_{\text{out}} T_{\text{ave}} - p_{\text{in}} T_{\text{ripple}}$$
(12)

where  $T_{\rm ave}$  and  $T_{\rm ripple}$  are the average torque and torque ripple components in the output torque, respectively. The analysis of  $T_{\rm ave}$  and  $T_{\rm ripple}$  is simplified when considering the partial derivatives of energy W with respect to  $\gamma$  and  $\eta$ .

The coordinate transformation is formulated as

$$\sqrt{p_{\text{in}}^2 + p_{\text{out}}^2} \begin{bmatrix} \cos(\delta) & -\sin(\delta) \\ \sin(\delta) & \cos(\delta) \end{bmatrix} \begin{bmatrix} \gamma \\ \eta \end{bmatrix} \\
= \begin{bmatrix} p_{\text{in}} & -p_{\text{out}} \\ p_{\text{out}} & p_{\text{in}} \end{bmatrix} \begin{bmatrix} \gamma \\ \eta \end{bmatrix} = \begin{bmatrix} \alpha \\ \beta \end{bmatrix} (13)$$

where  $tan(\delta) = -G_r$ .

Insertion of (7)–(13) into (6) gives

$$T_{\text{out}}(\gamma, \eta) = \sum_{m_1=1,3,5...}^{+\infty} \sum_{m_2=1,3,5...}^{+\infty} a_{m_1,m_2} f_1''$$

$$+ \sum_{n_1=1,3,5...}^{+\infty} \sum_{n_2=1,3,5...}^{+\infty} a_{n_1,n_2} f_2''$$

$$+ \sum_{m_1=1,3,5...}^{+\infty} \sum_{n_2=1,3,5...}^{+\infty} a_{m_2,n_2} f_3'' \qquad (14)$$

where  $a_{\cdot,\cdot}$  are the coefficients of the associated waveforms  $f_i''$ . The derivation of waveforms  $f_i''$  has been detailed in the Appendix. The waveforms in the output torque in terms of  $\gamma$  and  $\eta$  are listed as follows:

1) Under the condition  $(m_1 \pm m_2)p_{in} = kp_{mod}$ 

$$f_1'' = \sin \left\{ (m_1 \pm m_2) p_{\text{in}}^2 \gamma - (m_1 \pm m_2) p_{\text{in}} p_{\text{out}} \eta \right\}.$$
 (15)

2) Under the condition  $(n_1 \pm n_2) p_{\text{out}} = k p_{\text{mod}}$ 

$$f_2'' = \sin \{ (n_1 \pm n_2) p_{\text{out}}^2 \gamma + (n_1 \pm n_2) p_{\text{in}} p_{\text{out}} \eta \}.$$
 (16)

3) Under the condition  $mp_{\rm in} \pm np_{\rm out} = kp_{\rm mod}$ 

$$f_3'' = \sin \{ (mp_{\text{in}}^2 \pm np_{\text{out}}^2) \gamma - (m \mp n) p_{\text{in}} p_{\text{out}} \eta \}.$$
 (17)

Here, k is an integer,  $m_i$  and  $n_i$  are positive odd numbers.

Similar to the above discussion, the input torque can be written as

$$T_{\rm in} = -\frac{\partial W(\alpha, \beta)}{\partial \alpha} = -\frac{\partial W(\gamma, \eta)}{\partial \gamma} \frac{\partial \gamma}{\partial \alpha} - \frac{\partial W(\gamma, \eta)}{\partial \eta} \frac{\partial \eta}{\partial \alpha}$$
$$= -p_{\rm in} \frac{\partial W(\gamma, \eta)}{\partial \gamma} + p_{\rm out} \frac{\partial W(\gamma, \eta)}{\partial \eta}$$
$$= -p_{\rm in} T_{\rm ave} + p_{\rm out} T_{\rm ripple}. \tag{18}$$

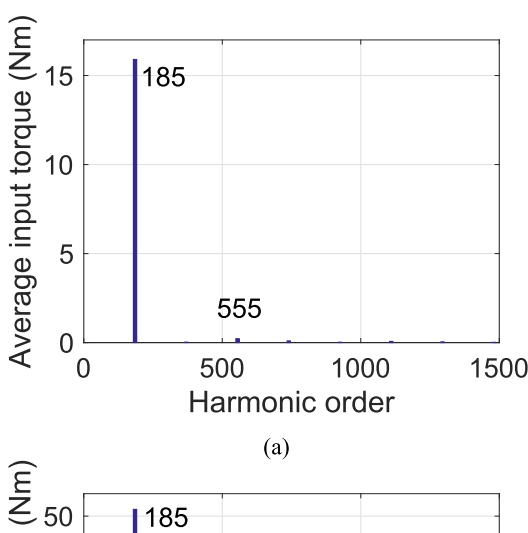
In this case, the magnetic energy W is stored in the inner air gap and can be calculated by substituting  $t_{\rm gap} = R_{\rm iom} - R_{\rm iim}$  and  $r = (R_{\rm if} + R_{\rm iom})/2$  into (7). The input torque and output torque share the same expression of magnetic flux distribution  $\vec{\phi}$ , as shown in (8). Hence,  $T_{\rm ave}$  and  $T_{\rm ripple}$  are equivalent to the input torque and output torque in the  $\gamma - \eta$  coordinate system.

#### C. Average Torque Analysis

The harmonics in the average torque, which are represented by the  $\gamma$ -axis, are identified by substituting  $\eta=0$  into (15)–(17). Table III shows the constraints and corresponding order numbers of the average torque. The lowest order of

TABLE III  $\label{table iii} \mbox{Harmonics in the Average Torque as Predicted} \\ \mbox{ by the Analytical Model}$ 

Order	Constraint	Value of order in this study
$(m_1 \pm m_2)p_{in}^2$	$(m_1 \pm m_2)p_{in} = kp_{mod}$	544, 1088,
$(n_1 \pm n_2)p_{out}^2$	$(n_1 \pm n_2)p_{out} = kp_{mod}$	5746, 11492,
$mp_{in}^2 \pm np_{out}^2$	$mp_{in} \pm np_{out} = kp_{mod}$	185, 370, 555



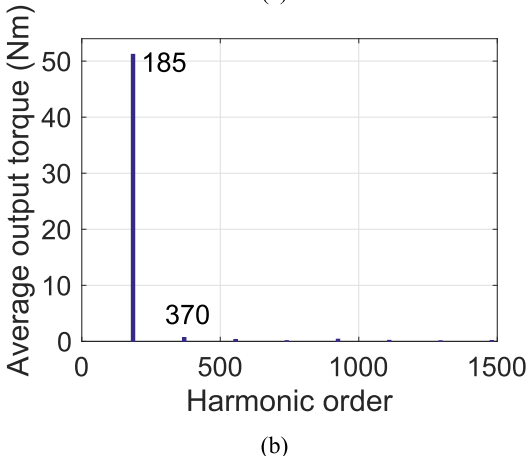


Fig. 9. FFT of (a) input torque  $T_{\rm in}$  and (b) output torque  $T_{\rm out}$  with respect to the average torque argument  $\gamma$ , based on the 2-D FE model.

the average torque is  $p_{\rm in}^2 + p_{\rm out}^2 = 185$ , which corresponds to a period of  $2\pi/(p_{\rm in}^2 + p_{\rm out}^2)$  in the  $\gamma$  direction.

For the specific CMG presented in Fig. 2, the average torque  $T_{\rm ave}$  is calculated via a 2-D FE model by setting  $\eta=0$  and varying  $\gamma$  from  $-\pi/(p_{\rm in}^2+p_{\rm out}^2)$  to  $\pi/(p_{\rm in}^2+p_{\rm out}^2)$  in 1024 steps. The fast Fourier transform (FFT) of  $T_{\rm ave}$  with respect to  $\gamma$  is presented in Fig. 9. The horizontal axis of the FFT result is normalized with respect to  $2\pi$  such that its values directly correspond to the order values. The harmonics of  $T_{\rm ave}$  predicted by the FE model agree with those of the analytical analysis.

For a given torsional load  $T_{\text{load}}$ , the equilibrium position of the CMG can be obtained by solving  $T_{\text{out}}(\gamma, \eta = 0) = T_{\text{load}}$ . The relative slipping of the rings when the CMG is overloaded can be analyzed along the  $\gamma$  direction. The CMG will keep operating along the  $\gamma$  direction until the torsional

TABLE IV

HARMONICS IN THE TORQUE RIPPLES AS PREDICTED

BY THE ANALYTICAL MODEL

Order (greater than 0)	Constraint	Value of order in this study
$(m_1 \pm m_2)p_{in}p_{out}$	$(m_1 \pm m_2)p_{in} = kp_{mod}$	1768, 3536,
$(n_1 \pm n_2)p_{in}p_{out}$	$(n_1 \pm n_2)p_{out} = kp_{mod}$	1768, 3536,
$(m \mp n)p_{in}p_{out}$	$mp_{in} \pm np_{out} = kp_{mod}$	1768, 3536,

load becomes smaller than the maximum output torque and a new equilibrium position is reached.

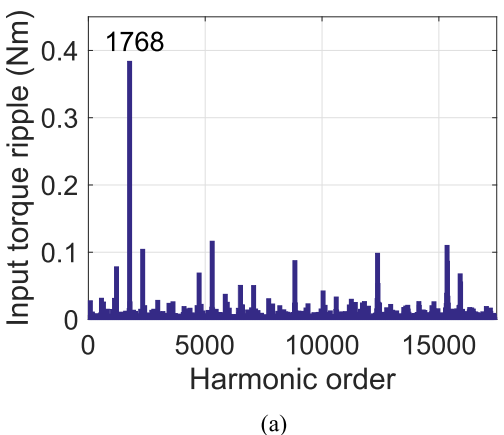
## D. Torque Ripple Analysis

The harmonics of the torque ripples, which are represented by the  $\eta$ -axis, are identified by substituting  $\gamma=0$  into (15)–(17). Table IV shows the constraints and corresponding order numbers of the torque ripples. The lowest harmonic order of the torque ripples is  $2p_{\text{mod}}p_{\text{in}}p_{\text{out}}=1768$ , which corresponds to a period of  $\pi/p_{\text{mod}}p_{\text{in}}p_{\text{out}}$  in the  $\eta$  direction.

Similar to the average torque analysis, the torque ripples component  $T_{\text{ripple}}$  is calculated from the 2-D FE model by setting  $\gamma=0$  and varying  $\eta$  from  $-\pi/(2p_{\text{mod}}p_{\text{in}}p_{\text{out}})$  to  $\pi/(2p_{\text{mod}}p_{\text{in}}p_{\text{out}})$  in 2048 steps. The FFT of  $T_{\text{ripple}}$  with respect to  $\eta$  is presented in Fig. 10. The horizontal axis of the FFT result is normalized with respect to  $2\pi$  such that its values directly correspond to the order values. The harmonics of  $T_{\text{ripple}}$  predicted by the FE model again match those of the analytical analysis.

## E. Torque Surface Method in the $\gamma - \eta$ Coordinate System

In this paper,  $p_{in}$  and  $p_{out}$  are the coprime integers. Thus, the CMG returns back to the original position when the inner ring rotates by  $p_{\text{out}}$  turns and the outer ring rotates by  $p_{\text{in}}$ turns. In order to achieve the complete torque surface in the  $\alpha - \beta$  coordinate system, a large sweep region, in which  $\alpha$  varies from 0 to  $2\pi p_{\text{out}}$  and  $\beta$  varies from 0 to  $2\pi p_{\text{in}}$ , is required. The sweep region can be greatly shrunk in the  $\gamma - \eta$  coordinate system. According to Sections V-C and V-D, the lowest order along the  $\eta$ -axis is  $2p_{\rm in}p_{\rm out}$ . Thus, the minimum sweep range along the  $\eta$ -axis is  $\pi/p_{\rm in}p_{\rm out}$ . Similarly, the sweeping range along the  $\gamma$ -axis is  $2\pi (p_{\rm in}^2 + p_{\rm out}^2)$ . For the CMG in this paper, the first harmonic of  $\gamma$  dominates and thus the sweep range for  $\gamma$  can be further reduced to  $(p_{\rm in}^2 + p_{\rm out}^2)\pi/2$ . Both the torque ripples and load dependence of the CMG can be conveniently obtained from the torque surface presented in Fig. 11. The torque ripples associated with a given average output torque of 51 N·m, which corresponds to  $\gamma = -1.35 \times 10^{-4}$ , can be obtained from the intersection between the torque surface and a vertical plane perpendicular to the  $\gamma - \eta$  plane. The other intersection between the torque surface and a horizontal torque plane, which represents a constant torque of  $T_{\text{out}}^{2-D} = 20 \text{ N·m}$ , indicates the rotation speed fluctuation in the outer ring when the torsional load is controlled to be 20 N·m. In this paper, both the torque ripples and speed fluctuation of the proposed CMG are negligible



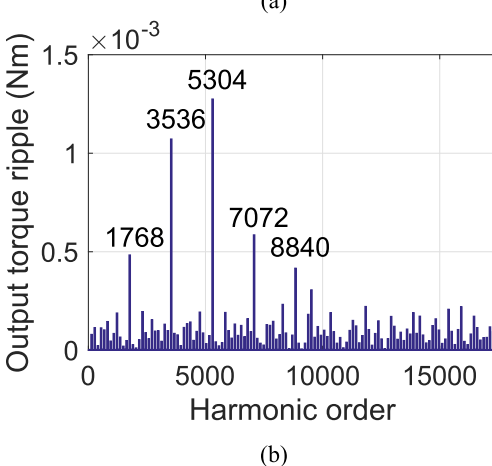


Fig. 10. FFT of (a) input torque  $T_{\rm in}$  and (b) output torque  $T_{\rm out}$  with respect to the *torque ripple argument*  $\eta$ , based on the 2-D FE model.

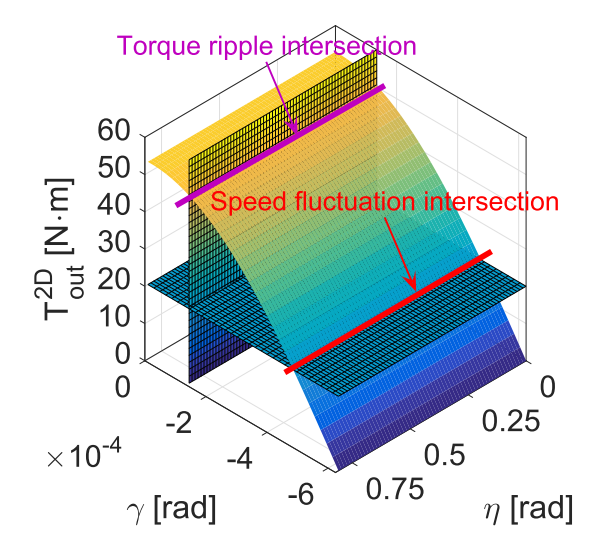


Fig. 11. Torque surface obtained from the minimum sweep ranges in the  $\gamma - \eta$  coordinate system. Purple intersection: torque ripples on the outer ring when the equilibrium position of the CMG is  $\gamma = -1.35 \times 10^{-4}$ . Red intersection: speed fluctuation on the outer ring when the output torque is controlled as a constant of 20 N·m.

due to the benefits of Halbach arrays and coprime magnetic pole numbers selected. Hence, the intersections presented in Fig. 11 are straight lines. However, the same method applies to other CMG configurations whose torque ripples and speed

fluctuations are large. This information is valuable for future control efforts to maintain constant output torque and speed.

### VI. CONCLUSION

This paper first investigates the influence of nonlinear magnetic material properties on the performance of a CMG. Magnetic saturation nonlinearities of the flux modulator are studied numerically by incorporating the JA model within FE frameworks. The nonlinear FE modeling results indicate that further increasing the initial magnetic permeability  $\mu_{r,in}$  and saturation flux density  $B_s$  of the soft magnetic flux modulator has negligible influence on the coupling torque, once they exceed the threshold values, which are  $\mu_{r,in} = 178$  and  $B_s = 1.55$  T for the given CMG design considered in this paper. The end effect of the CMG is then quantified in terms of a torque reduction ratio  $E_T$  by comparing the results of 2-D and 3-D FE models. A numerical study proves that end-effect losses are insensitive to the initial magnetic permeability. Similar to the coupling torque, the value of  $E_T$  remains constant at 65% once  $B_s$  exceeds the predetermined threshold value. Hence, the coupling torque of a CMG considering 3-D end-effect losses can be calculated efficiently via a 2-D FE model together with the correction constant  $E_T$ . This paper finally proposes a systematic torque surface method that decouples the analysis of average torque and torque ripples in CMGs. The torque surface, which describes all the possible operating conditions of a CMG, is obtained by sweeping the angular positions of the CMG in FE modeling. The harmonics in the average torque and the torque ripples are derived analytically. The analytical results agree well with those obtained from the torque surface method. Based on the analytical model, the efficiency of the torque surface method is further improved by reducing the sweep ranges of selected parameters. The speed fluctuations for static or low-frequency applications, where inertial effects are negligible compared to loads, at given constant torsional loads can be efficiently and accurately obtained from the reduced torque surface.

APPENDIX—WAVEFORMS IN THE COUPLING TORQUE

According to (7), the magnetic energy stored in the air gap is

$$W(\alpha, \beta) = C_0 \int_0^{2\pi} |\phi(r_{\text{gap,out}}, \theta)|^2 d\theta$$
 (19)

where  $C_0$  is a constant coefficient associated with the CMG geometry. The magnitude of  $|\phi(r_{\rm gap,out},\theta)|^2$ , as presented in (20), is obatained by substituting (9)–(11) into (8)

$$|\phi(r_{\text{gap,out}}, \theta)|^{2}$$

$$= a_{l0}^{2} \sum_{m_{1}=1,3...}^{\infty} \sum_{m_{2}=1,3...}^{\infty} a_{m_{1}}$$

$$\times a_{m_{2}} \underbrace{\sin[m_{1}p_{\text{in}}(\theta + \alpha)] \sin[m_{2}p_{\text{in}}(\theta + \alpha)]}_{2f_{1}}$$

$$+ a_{l0}^{2} \sum_{m_{1}=1,3...}^{\infty} \sum_{n_{2}=1,3...}^{\infty} a_{n_{1}}$$

$$\times a_{n_{2}} \underbrace{\sin[n_{1}p_{\text{out}}(\theta + \beta)] \sin[n_{2}p_{\text{out}}(\theta + \beta)]}_{2f_{2}}$$

$$+ 2a_{l0}^{2} \sum_{m=1,3...}^{\infty} \sum_{n=1,3...}^{\infty} a_{m}$$

$$\times a_{n} \underbrace{\sin[mp_{\text{in}}(\theta + \alpha)] \sin[np_{\text{out}}(\theta + \beta)]}_{2f_{3}}$$

$$+ 2a_{l0} \sum_{m_{1}=1,3...}^{\infty} \sum_{m_{2}=1,3...}^{\infty} \sum_{l=1,3...}^{\infty} a_{l}a_{m_{1}}$$

$$\times a_{m_{2}} \underbrace{\sin[m_{1}p_{\text{in}}(\theta + \alpha)] \sin[m_{2}p_{\text{in}}(\theta + \alpha)] \sin[lp_{\text{mod}}\theta)}_{4f_{4}}$$

$$+ 2a_{l0} \sum_{n_{1}=1,3...}^{\infty} \sum_{n_{2}=1,3...}^{\infty} \sum_{l=1,3...}^{\infty} a_{l}a_{n_{1}}$$

$$\times a_{n_{2}} \underbrace{\sin[n_{1}p_{\text{out}}(\theta + \beta)] \sin[n_{2}p_{\text{out}}(\theta + \beta)] \sin[lp_{\text{mod}}\theta)}_{4f_{5}}$$

$$+ 4a_{l0} \sum_{m=1,3...}^{\infty} \sum_{n=1,3...}^{\infty} \sum_{l=1,3...}^{\infty} a_{l}a_{m}$$

$$\times a_{n} \underbrace{\sin[mp_{\text{in}}(\theta + \alpha)] \sin[np_{\text{out}}(\theta + \beta)] \sin[lp_{\text{mod}}\theta)}_{4f_{6}}$$

$$+ \sum_{m_{1}=1,3...}^{\infty} \sum_{n_{2}=1,3...}^{\infty} \sum_{l=1,3...}^{\infty} \sum_{l_{2}=1,3...}^{\infty} a_{l_{1}}a_{l_{2}}a_{m_{1}}$$

$$\times a_{m_{2}} \underbrace{\sin[m_{1}p_{\text{in}}(\theta + \alpha)] \sin[np_{\text{out}}(\theta + \beta)] \sin[l_{1}p_{\text{mod}}\theta) \sin(l_{2}p_{\text{mod}}\theta)}_{8f_{7}}$$

$$+ \sum_{n_{1}=1,3...}^{\infty} \sum_{n_{2}=1,3...}^{\infty} \sum_{l_{1}=1,3....}^{\infty} \sum_{l_{2}=1,3...}^{\infty} a_{l_{1}}a_{l_{2}}a_{n_{1}}$$

$$\times a_{n_{2}} \underbrace{\sin[n_{1}p_{\text{out}}(\theta + \beta)] \sin[n_{2}p_{\text{out}}(\theta + \beta)] \sin(l_{1}p_{\text{mod}}\theta) \sin(l_{2}p_{\text{mod}}\theta)}_{8f_{8}}$$

$$+ 2 \sum_{m=1,3...}^{\infty} \sum_{n_{1}=1,3...}^{\infty} \sum_{l_{1}=1,3...}^{\infty} \sum_{l_{2}=1,3...}^{\infty} \sum_{l_{2}=1,3...}^{\infty} a_{l_{1}}a_{l_{2}}a_{m}$$

$$\times a_{n} \underbrace{\sin[mp_{\text{in}}(\theta + \alpha)] \sin[np_{\text{out}}(\theta + \beta)] \sin[np_{\text{out}}(\theta + \beta)] \sin(l_{1}p_{\text{mod}}\theta) \sin(l_{2}p_{\text{mod}}\theta)}_{8f_{9}}$$

$$\times a_{n} \underbrace{\sin[mp_{\text{in}}(\theta + \alpha)] \sin[np_{\text{out}}(\theta + \beta)] \sin[np_{\text{out}}(\theta + \beta)] \sin[lnp_{\text{out}}(\theta + \beta)] \sin[$$

By substituting (13) into (20), waveforms  $f_i$  can be converted into functions of  $\gamma$  and  $\eta$  as

$$f_{1} = \cos \left[ (m_{1} - m_{2}) p_{\text{in}} \theta + (m_{1} - m_{2}) p_{\text{in}}^{2} \gamma - (m_{1} - m_{2}) p_{\text{in}} p_{\text{out}} \eta \right]$$

$$- \cos \left[ (m_{1} + m_{2}) p_{\text{in}} \theta + (m_{1} + m_{2}) p_{\text{in}}^{2} \gamma - (m_{1} + m_{2}) p_{\text{in}} p_{\text{out}} \eta \right]$$

$$f_{2} = \cos \left[ (n_{1} - n_{2}) p_{\text{out}} \theta + (n_{1} - n_{2}) p_{\text{out}}^{2} \gamma + (n_{1} - n_{2}) p_{\text{in}} p_{\text{out}} \eta \right]$$

$$- \cos \left[ (n_{1} + n_{2}) p_{\text{out}} \theta + (n_{1} + n_{2}) p_{\text{out}}^{2} \gamma + (n_{1} + n_{2}) p_{\text{in}} p_{\text{out}} \eta \right]$$

$$f_{3} = \cos \left[ (m p_{\text{in}} - n p_{\text{out}}) \theta + (m p_{\text{in}}^{2} - n p_{\text{out}}^{2}) \gamma - (m + n) p_{\text{in}} p_{\text{out}} \eta \right]$$

$$- \cos \left[ (m p_{\text{in}} + n p_{\text{out}}) \theta + (m p_{\text{in}}^{2} + n p_{\text{out}}^{2}) \gamma - (m - n) p_{\text{in}} p_{\text{out}} \eta \right]$$

$$(23)$$

$$f_{4} = -\sin \left\{ \left[ (m_{1} - m_{2}) p_{\text{in}}^{-} - l p_{\text{mod}} \right] \theta \right. \\ + (m_{1} - m_{2}) p_{\text{in}}^{-} \gamma - (m_{1} - m_{2}) p_{\text{in}} p_{\text{out}} \eta \right] \\ + \sin \left\{ \left[ (m_{1} + m_{2}) p_{\text{in}}^{-} - l p_{\text{mod}} \right] \theta \right. \\ + (m_{1} + m_{2}) p_{\text{in}}^{-} \gamma - (m_{1} + m_{2}) p_{\text{in}} p_{\text{out}} \eta \right] \\ + \sin \left\{ \left[ (m_{1} - m_{2}) p_{\text{in}} + l p_{\text{mod}} \right] \theta \right. \\ + (m_{1} - m_{2}) p_{\text{in}}^{-} \gamma - (m_{1} - m_{2}) p_{\text{in}} p_{\text{out}} \eta \right] \\ - \sin \left\{ \left[ (m_{1} + m_{2}) p_{\text{in}} + l p_{\text{mod}} \right] \theta \right. \\ + (m_{1} + m_{2}) p_{\text{in}}^{-} \gamma - (m_{1} + m_{2}) p_{\text{in}} p_{\text{out}} \eta \right\} \\ - \sin \left\{ \left[ (m_{1} - n_{2}) p_{\text{out}} - l p_{\text{mod}} \right] \theta \right. \\ + (m_{1} - m_{2}) p_{\text{out}}^{-} \gamma + (n_{1} - n_{2}) p_{\text{in}} p_{\text{out}} \eta \right\} \\ + \sin \left\{ \left[ (m_{1} - n_{2}) p_{\text{out}} + l p_{\text{mod}} \right] \theta \right. \\ + (n_{1} + n_{2}) p_{\text{out}}^{-} \gamma + (n_{1} + n_{2}) p_{\text{in}} p_{\text{out}} \eta \right\} \\ + \sin \left\{ \left[ (m_{1} - n_{2}) p_{\text{out}} + l p_{\text{mod}} \right] \theta \right. \\ + (m_{1} - n_{2}) p_{\text{out}}^{-} \gamma + (n_{1} + n_{2}) p_{\text{in}} p_{\text{out}} \eta \right\} \\ - \sin \left\{ \left[ (m_{1} + n_{2}) p_{\text{out}} \gamma + (n_{1} + n_{2}) p_{\text{in}} p_{\text{out}} \eta \right] \right. \\ + \sin \left\{ (mp_{\text{in}} - np_{\text{out}} + l p_{\text{mod}} \right) \theta \right. \\ + (mp_{\text{in}}^{-} - np_{\text{out}}^{-} \gamma - (m + n) p_{\text{in}} p_{\text{out}} \eta \right\} \\ + \sin \left\{ (mp_{\text{in}} + np_{\text{out}} + l p_{\text{mod}} \right) \theta \\ + (mp_{\text{in}}^{-} - np_{\text{out}}^{-} \gamma - (m + n) p_{\text{in}} p_{\text{out}} \eta \right\} \\ + \sin \left\{ (mp_{\text{in}} + np_{\text{out}} + l p_{\text{mod}} \right) \theta \\ + (mp_{\text{in}}^{-} - np_{\text{out}}^{-} \gamma - (m + n) p_{\text{in}} p_{\text{out}} \eta \right\} \\ + \sin \left\{ (mp_{\text{in}} + np_{\text{out}} + l p_{\text{mod}} \right) \theta \\ + (mp_{\text{in}}^{-} - np_{\text{out}}^{-} \gamma - (m + n) p_{\text{in}} p_{\text{out}} \eta \right\} \\ + \sin \left\{ (mp_{\text{in}} + np_{\text{out}} + l p_{\text{mod}} \right) \theta \\ + (mp_{\text{in}}^{-} - np_{\text{out}}^{-} \gamma - (m + n) p_{\text{in}} p_{\text{out}} \eta \right\} \\ + \sin \left\{ (mp_{\text{in}} + np_{\text{out}}^{-} \gamma - (m + n) p_{\text{in}} p_{\text{out}} \eta \right\} \\ + \sin \left\{ (mp_{\text{in}} + m_{2}) p_{\text{in}}^{-} \gamma - (m + m_{2}) p_{\text{in}} p_{\text{out}} \eta \right\} \\ + \sin \left\{ (mp_{\text{in}} + m_{2}) p_{\text{in}}^{-} \gamma - (m + m_{2}) p_{\text{in}} p_{\text{out}} \eta \right\} \\ - \sin \left\{ (mp_{\text{in}} + m_{2}) p_{\text{in}}^{-}$$

+  $\sin \{ [(n_1 - n_2)p_{\text{out}} + (l_1 - l_2)p_{\text{mod}}] \theta$ 

$$+ (n_1 - n_2) p_{\text{out}}^2 \gamma + (n_1 - n_2) p_{\text{in}} p_{\text{out}} \eta$$

$$- \sin \left\{ [(n_1 + n_2) p_{\text{out}} \gamma + (n_1 + n_2) p_{\text{in}} p_{\text{out}} \eta \right\}$$

$$+ (n_1 + n_2) p_{\text{out}}^2 \gamma + (n_1 + n_2) p_{\text{in}} p_{\text{out}} \eta$$

$$+ \sin \left\{ [(n_1 - n_2) p_{\text{out}} \gamma + (n_1 - n_2) p_{\text{in}} p_{\text{out}} \eta \right\}$$

$$+ \sin \left\{ [(n_1 - n_2) p_{\text{out}} \gamma + (n_1 - n_2) p_{\text{in}} p_{\text{out}} \eta \right\}$$

$$- \sin \left\{ [(n_1 + n_2) p_{\text{out}} \gamma + (n_1 + n_2) p_{\text{in}} p_{\text{out}} \eta \right\}$$

$$- \sin \left\{ [(n_1 + n_2) p_{\text{out}} \gamma + (n_1 + n_2) p_{\text{in}} p_{\text{out}} \eta \right\}$$

$$- \sin \left\{ [(n_1 - n_2) p_{\text{out}} \gamma + (n_1 - n_2) p_{\text{in}} p_{\text{out}} \eta \right\}$$

$$+ \sin \left\{ [(n_1 + n_2) p_{\text{out}} \gamma + (n_1 + n_2) p_{\text{in}} p_{\text{out}} \eta \right\}$$

$$+ \sin \left\{ [(n_1 + n_2) p_{\text{out}} \gamma + (n_1 + n_2) p_{\text{in}} p_{\text{out}} \eta \right\}$$

$$+ \sin \left\{ [(n_1 + n_2) p_{\text{out}} \gamma + (n_1 + n_2) p_{\text{in}} p_{\text{out}} \eta \right\}$$

$$+ \sin \left\{ [m p_{\text{in}} - n p_{\text{out}} - (l_1 + l_2) p_{\text{mod}}] \theta \right\}$$

$$+ (m p_{\text{in}}^2 - n p_{\text{out}}^2) \gamma - (m + n) p_{\text{in}} p_{\text{out}} \eta \right\}$$

$$+ \sin \left\{ [m p_{\text{in}} - n p_{\text{out}} + (l_1 - l_2) p_{\text{mod}}] \theta \right\}$$

$$+ (m p_{\text{in}}^2 - n p_{\text{out}}^2) \gamma - (m + n) p_{\text{in}} p_{\text{out}} \eta \right\}$$

$$+ \sin \left\{ [m p_{\text{in}} - n p_{\text{out}} + (l_1 - l_2) p_{\text{mod}}] \theta \right\}$$

$$+ (m p_{\text{in}}^2 - n p_{\text{out}}^2) \gamma - (m + n) p_{\text{in}} p_{\text{out}} \eta \right\}$$

$$- \sin \left\{ [m p_{\text{in}} - n p_{\text{out}} - (l_1 - l_2) p_{\text{mod}}] \theta \right\}$$

$$+ (m p_{\text{in}}^2 - n p_{\text{out}}^2) \gamma - (m + n) p_{\text{in}} p_{\text{out}} \eta \right\}$$

$$- \sin \left\{ [m p_{\text{in}} - n p_{\text{out}} - (l_1 - l_2) p_{\text{mod}}] \theta \right\}$$

$$+ (m p_{\text{in}}^2 - n p_{\text{out}}^2) \gamma - (m - n) p_{\text{in}} p_{\text{out}} \eta \right\}$$

$$- \sin \left\{ [m p_{\text{in}} - n p_{\text{out}} - (l_1 - l_2) p_{\text{mod}}] \theta \right\}$$

$$+ (m p_{\text{in}}^2 - n p_{\text{out}}^2) \gamma - (m - n) p_{\text{in}} p_{\text{out}} \eta \right\}$$

$$+ \sin \left\{ [m p_{\text{in}} - n p_{\text{out}} + (l_1 + l_2) p_{\text{mod}}] \theta \right\}$$

$$+ (m p_{\text{in}}^2 - n p_{\text{out}}^2) \gamma - (m - n) p_{\text{in}} p_{\text{out}} \eta \right\}$$

$$+ \sin \left\{ [m p_{\text{in}} - n p_{\text{out}} + (l_1 + l_2) p_{\text{mod}}] \theta \right\}$$

$$+ (m p_{\text{in}}^2 - n p_{\text{out}}^2) \gamma - (m - n) p_{\text{in}} p_{\text{out}} \eta \right\}$$

$$+ \sin \left\{ [m p_{\text{in}} - n p_{\text{out}}$$

or alternatively

$$f_{1} = \cos \left[ (m_{1} \pm m_{2}) p_{\text{in}} \theta + (m_{1} \pm m_{2}) p_{\text{in}}^{2} \gamma - (m_{1} \pm m_{2}) p_{\text{out}} \eta \right]$$
(30)  

$$f_{2} = \cos \left[ (n_{1} \pm n_{2}) p_{\text{out}} \theta + (n_{1} \pm n_{2}) p_{\text{out}}^{2} \gamma + (n_{1} \pm n_{2}) p_{\text{in}} p_{\text{out}} \eta \right]$$
(31)  

$$f_{3} = \cos \left[ (m p_{\text{in}} \pm n p_{\text{out}}) \theta + (m p_{\text{in}}^{2} \pm n p_{\text{out}}^{2}) \gamma - (m \mp n) p_{\text{in}} p_{\text{out}} \eta \right]$$
(32)  

$$f_{4} = \sin \left\{ \left[ (m_{1} \pm m_{2}) p_{\text{in}} - l p_{\text{mod}} \right] \theta + (m_{1} \pm m_{2}) p_{\text{in}}^{2} \gamma - (m_{1} \pm m_{2}) p_{\text{in}} p_{\text{out}} \eta \right\}$$
(33)  

$$+ \sin \left\{ \left[ (m_{1} \pm m_{2}) p_{\text{in}} + l p_{\text{mod}} \right] \theta + (m_{1} \pm m_{2}) p_{\text{out}}^{2} \gamma - (m_{1} \pm m_{2}) p_{\text{in}} p_{\text{out}} \eta \right\}$$
(33)  

$$f_{5} = \sin \left\{ \left[ (n_{1} \pm n_{2}) p_{\text{out}} - l p_{\text{mod}} \right] \theta + (n_{1} \pm n_{2}) p_{\text{out}}^{2} \gamma + (n_{1} \pm n_{2}) p_{\text{in}} p_{\text{out}} \eta \right\}$$
(34)  

$$+ \sin \left\{ \left[ (n_{1} \pm n_{2}) p_{\text{out}} + l p_{\text{mod}} \right] \theta + (m p_{\text{in}}^{2} \pm n p_{\text{out}}^{2}) \gamma - (m \mp n) p_{\text{in}} p_{\text{out}} \eta \right\}$$
(34)

$$+ \sin \left\{ (mp_{\text{in}} \pm np_{\text{out}} + lp_{\text{mod}})\theta + (mp_{\text{in}}^2 \pm np_{\text{out}}^2)\gamma - (m \mp n)p_{\text{in}}p_{\text{out}}\eta \right\}$$
(35)  

$$f_7 = \sin \left\{ [(m_1 \pm m_2)p_{\text{in}} - (l_1 + l_2)p_{\text{mod}}]\theta + (m_1 \pm m_2)p_{\text{in}}\gamma - (m_1 \pm m_2)p_{\text{in}}p_{\text{out}}\eta \right\}$$

$$+ \sin \left\{ [(m_1 \pm m_2)p_{\text{in}} - (l_1 - l_2)p_{\text{mod}}]\theta + (m_1 \pm m_2)p_{\text{in}}\gamma - (m_1 \pm m_2)p_{\text{in}}p_{\text{out}}\eta \right\}$$

$$+ \sin \left\{ [(m_1 \pm m_2)p_{\text{in}} + (l_1 - l_2)p_{\text{mod}}]\theta + (m_1 \pm m_2)p_{\text{in}}\gamma - (m_1 \pm m_2)p_{\text{in}}p_{\text{out}}\eta \right\}$$

$$+ \sin \left\{ [(m_1 \pm m_2)p_{\text{in}}\gamma - (m_1 \pm m_2)p_{\text{in}}p_{\text{out}}\eta \right\}$$

$$+ (m_1 \pm m_2)p_{\text{in}}^2\gamma - (m_1 \pm m_2)p_{\text{in}}p_{\text{out}}\eta \right\}$$
(36)

$$f_{8} = \sin \left\{ [(n_{1} \pm n_{2})p_{\text{out}} - (l_{1} + l_{2})p_{\text{mod}}]\theta + (n_{1} \pm n_{2})p_{\text{out}}\gamma + (n_{1} \pm n_{2})p_{\text{in}}p_{\text{out}}\eta \right\}$$

$$+ \sin \left\{ [(n_{1} \pm n_{2})p_{\text{out}} - (l_{1} - l_{2})p_{\text{mod}}]\theta + (n_{1} \pm n_{2})p_{\text{out}}\gamma + (n_{1} \pm n_{2})p_{\text{in}}p_{\text{out}}\eta \right\}$$

$$+ \sin \left\{ [(n_{1} \pm n_{2})p_{\text{out}}\gamma + (n_{1} \pm n_{2})p_{\text{in}}p_{\text{out}}\eta \right\}$$

$$+ \sin \left\{ [(n_{1} \pm n_{2})p_{\text{out}}\gamma + (n_{1} \pm n_{2})p_{\text{in}}p_{\text{out}}\eta \right\}$$

$$+ \sin \left\{ [(n_{1} \pm n_{2})p_{\text{out}}\gamma + (n_{1} \pm n_{2})p_{\text{in}}p_{\text{out}}\eta \right\}$$

$$+ \sin \left\{ [(n_{1} \pm n_{2})p_{\text{out}}\gamma + (n_{1} \pm n_{2})p_{\text{in}}p_{\text{out}}\eta \right\}$$

$$+ (n_{1} \pm n_{2})p_{\text{out}}\gamma + (n_{1} \pm n_{2})p_{\text{in}}p_{\text{out}}\eta \right\}$$

$$+ (m_{1} \pm n_{2})p_{\text{out}}\gamma - (n_{1} \pm n_{2})p_{\text{in}}p_{\text{out}}\eta \}$$

$$+ \sin \left\{ [mp_{\text{in}} \pm np_{\text{out}} - (l_{1} - l_{2})p_{\text{mod}}]\theta + (mp_{\text{in}}^{2} \pm np_{\text{out}}^{2})\gamma - (m \mp n)p_{\text{in}}p_{\text{out}}\eta \right\}$$

$$+ \sin \left\{ [mp_{\text{in}} \pm np_{\text{out}} + (l_{1} - l_{2})p_{\text{mod}}]\theta + (mp_{\text{in}}^{2} \pm np_{\text{out}}^{2})\gamma - (m \mp n)p_{\text{in}}p_{\text{out}}\eta \right\}$$

$$+ \sin \left\{ [mp_{\text{in}} \pm np_{\text{out}} + (l_{1} + l_{2})p_{\text{mod}}]\theta + (mp_{\text{in}}^{2} \pm np_{\text{out}}^{2})\gamma - (m \mp n)p_{\text{in}}p_{\text{out}}\eta \right\} .$$

$$(38)$$

The waveforms  $f_1$ ,  $f_4$ , and  $f_7$  can be merged as

$$f_1' = \sin \left\{ [(m_1 \pm m_2)p_{\rm in} - kp_{\rm mod}]\theta + (m_1 \pm m_2)p_{\rm in}^2\gamma - (m_1 \pm m_2)p_{\rm in}p_{\rm out}\eta \right\}$$
(39)

where k is an integer. The waveform of  $f_1$  shown in (30) corresponds to the case when k=0; the waveform of  $f_4$  shown in (33) corresponds to the case when k is an odd number; the waveform of  $f_7$  shown in (36) corresponds to the case when k is an even number. Similarly, (31), (34), and (37) can be merged as

$$f_2' = \sin \left\{ [(n_1 \pm n_2) p_{\text{out}} - k p_{\text{mod}}] \theta + (n_1 \pm n_2) p_{\text{out}}^2 \gamma + (n_1 \pm n_2) p_{\text{in}} p_{\text{out}} \eta \right\}.$$
(40)

Equations (32), (35), and (38) are simplified into

$$f_3' = \sin \left\{ (mp_{\text{in}} \pm np_{\text{out}} - kp_{\text{mod}})\theta + (mp_{\text{in}}^2 \pm np_{\text{out}}^2)\gamma - (m \mp n)p_{\text{in}}p_{\text{out}}\eta \right\}.$$
(41)

Considering the integration in (7) with the trigonometric relations

$$\int_0^{2\pi} \sin(a\theta + b)d\theta = \begin{cases} 0 & \text{if } a \neq 0\\ 2\pi \sin(b) & \text{if } a = 0 \end{cases}$$
 (42)

and

$$\int_0^{2\pi} \cos(a\theta + b)d\theta = \begin{cases} 0 & \text{if } a \neq 0 \\ 2\pi \cos(b) & \text{if } a = 0 \end{cases}$$
 (43)

waveforms in (39)–(41) produce non-zero magnetic energy  $W(\alpha, \beta)$  if and only if the coefficients of  $\theta$  are zero. Thus, the waveforms eventually reduce to (15)–(17) under the aforementioned conditions.

#### ACKNOWLEDGMENT

We wish to acknowledge the member organizations of the Smart Vehicle Concepts Center, a National Science Foundation Industry-University Cooperative Research Center (www.SmartVehicleCenter.org) established under NSF Grant IIP-1238286. Financial support from NASA's Revolutionary Vertical Lift Technology Project and the Independent Research and Development Program is acknowledged.

## REFERENCES

- K. Ikuta, S. Makita, and S. Arimoto, "Non-contact magnetic gear for micro transmission mechanism," in *Proc. IEEE Micro Conf. Electro Mech. Syst.*, Nara, Japan, Jan. 1991, pp. 125–130.
- [2] H. T. Faus, "Magnet gearing," U.S. Patent 2243555 A, May 27, 1941.
- [3] F. T. Jorgensen, T. O. Andersen, and P. O. Rasmussen, "The cycloid permanent magnetic gear," *IEEE Trans. Ind. Appl.*, vol. 44, no. 6, pp. 1659–1665, Nov. 2008.
- [4] J. Rens, R. Clark, S. Calverley, K. Atallah, and D. Howe, "Design, analysis and realization of a novel magnetic harmonic gear," in *Proc. 18th Int. Conf. Elect. Mach. (ICEM)*, Sep. 2008, pp. 1–4.
- [5] S. Pakdelian, N. W. Frank, and H. A. Toliyat, "Principles of the transrotary magnetic gear," *IEEE Trans. Mgn.*, vol. 49, no. 2, pp. 883–889, Feb. 2013.
- [6] S. Pakdelian, N. W. Frank, and H. A. Toliyat, "Magnetic design aspects of the trans-rotary magnetic gear," *IEEE Trans. Energy Convers.*, vol. 30, no. 1, pp. 41–50, Mar. 2015.
- [7] T. B. Martin, Jr., "Magnetic transmission," U.S. Patent 3378710 A, Apr. 16, 1968.
- [8] K. Atallah and D. Howe, "A novel high-performance magnetic gear," IEEE Trans. Magn., vol. 37, no. 4, pp. 2844–2846, Jul. 2001.
- [9] G. Puchhammer, "Magnetic gearing versus conventional gearing in actuators for aerospace applications," in *Proc. 42nd Aerosp. Mech.* Symp., May 2014, pp. 175–182.
- [10] E. Gouda, S. Mezani, L. Baghli, and A. Rezzoug, "Comparative study between mechanical and magnetic planetary gears," *IEEE Trans. Magn.*, vol. 47, no. 2, pp. 439–450, Feb. 2011.
- [11] K. Atallah, J. Wang, S. D. Calverley, and S. Duggan, "Design and operation of a magnetic continuously variable transmission," *IEEE Trans. Ind. Appl.*, vol. 48, no. 4, pp. 1288–1295, Jul. 2012.
- [12] H. Shin and J. Chang, "Comparison of radial force at modulating pieces in coaxial magnetic gear and magnetic geared machine," *IEEE Trans. Magn.*, vol. 54, no. 3, Mar. 2018, Art. no. 8101904.
- [13] K. Aiso, K. Akatsu, and Y. Aoyama, "A novel magnetic gear for high speed motor system," in *Proc. IEEE Int. Elect. Mach. Drives* Conf. (IEMDC), May 2017, pp. 1–7.
- [14] G. Jungmayr, J. Loeffler, B. Winter, F. Jeske, and W. Amrhein, "Magnetic gear: Radial force, cogging torque, skewing and optimization," in *Proc. IEEE Energy Convers. Congr. Expo.*, Sep. 2015, pp. 898–905.
- [15] D. Žarko, D. Ban, and T. A. Lipo, "Analytical calculation of magnetic field distribution in the slotted air gap of a surface permanent-magnet motor using complex relative air-gap permeance," *IEEE Trans. Magn.*, vol. 42, no. 7, pp. 1828–1837, Jul. 2006.
- [16] Z. Q. Zhu and D. Howe, "Instantaneous magnetic field distribution in brushless permanent magnet DC motors. III. Effect of stator slotting," *IEEE Trans. Magn.*, vol. 29, no. 1, pp. 143–151, Jan. 1993.
- [17] K. Atallah, S. D. Calverley, and D. Howe, "Design, analysis and realisation of a high-performance magnetic gear," *IEE Proc. Elect. Power Appl.*, vol. 151, no. 2, pp. 135–143, Mar. 2004.
  [18] L. Jian and K. T. Chau, "A coaxial magnetic gear with Halbach
- [18] L. Jian and K. T. Chau, "A coaxial magnetic gear with Halbach permanent-magnet arrays," *IEEE Trans. Energy Convers.*, vol. 25, no. 2, pp. 319–328, Jun. 2010.

- [19] N. Niguchi and K. Hirata, "Cogging torque analysis of magnetic gear," IEEE Trans. Ind. Electron., vol. 59, no. 5, pp. 2189–2197, May 2012.
- [20] M. Fukuoka, K. Nakamura, and O. Ichinokura, "Dynamic analysis of planetary-type magnetic gear based on reluctance network analysis," *IEEE Trans. Magn.*, vol. 47, no. 10, pp. 2414–2417, Oct. 2011.
- [21] M. Fukuoka, K. Nakamura, and O. Ichinokura, "A method for optimizing the design of SPM type magnetic gear based on reluctance network analysis," in *Proc. 40th Int. Conf. Elect. Mach.*, Sep. 2012, pp. 30–35.
- [22] M. Johnson, M. C. Gardner, and H. A. Toliyat, "A parameterized linear magnetic equivalent circuit for analysis and design of radial flux magnetic gears—Part I: Implementation," *IEEE Trans. Energy Convers.*, vol. 33, no. 2, pp. 784–791, Jun. 2018.
- [23] M. Desvaux, B. Traullé, R. L. G. Latimier, S. Sire, B. Multon, and H. B. Ahmed, "Computation time analysis of the magnetic gear analytical model," *IEEE Trans. Magn.*, vol. 53, no. 5, May 2017, Art. no. 7000409.
- [24] Y.-J. Ge, C.-Y. Nie, and Q. Xin, "A three dimensional analytical calculation of the air-gap magnetic field and torque of coaxial magnetic gears," *Prog. Electromagn. Res.*, vol. 131, pp. 391–407, Jan. 2012.
- [25] P. O. Rasmussen, T. O. Andersen, F. T. Joergensen, and O. Nielsen, "Development of a high performance magnetic gear," in *Proc. 38th IAS Annu. Meeting Conf. Rec. Ind. Appl. Conf.*, vol. 3, Oct. 2003, pp. 1696–1702.

- [26] L. Jian, K. T. Chau, Y. Gong, J. Z. Jiang, C. Yu, and W. Li, "Comparison of coaxial magnetic gears with different topologies," *IEEE Trans. Magn.*, vol. 45, no. 10, pp. 4526–4529, Oct. 2009.
- [27] S. Gerber and R.-J. Wang, "Analysis of the end-effects in magnetic gears and magnetically geared machines," in *Proc. Int. Conf. Elect. Mach. (ICEM)*, Sep. 2014, pp. 396–402.
- [28] Y. B. Li, S. Niu, S. L. Ho, Y. Li, and W. N. Fu, "Hysteresis effects of laminated steel materials on detent torque in permanent magnet motors," *IEEE Trans. Magn.*, vol. 47, no. 10, pp. 3594–3597, Oct. 2011.
- [29] M. Filippini, P. Alotto, G. Glehn, and K. Hameyer, "Magnetic transmission gear finite element simulation with iron pole hysteresis," *Open Phys.*, vol. 16, no. 1, pp. 105–110, 2018.
- [30] D. C. Jiles and D. L. Atherton, "Theory of ferromagnetic hysteresis," J. Magn. Magn. Mater., vol. 61, nos. 1–2, pp. 48–60, Sep. 1986.
- [31] D. K. Rao. (Mar. 8, 2018). MagWeb User Manual. [Online]. Available: https://magweb-website-magwebusa.netdna-ssl.com/wp-content/ uploads/2018/03/User-Manual-Version-4.pdf
- [32] Magnetics, Division of Spang & Co. (May 8, 2018). Supermalloy Material Property Curves. [Online]. Available: https://www.mag-inc.com/Products/Tape-Wound-Cores/Supermalloy/Supermalloy-Material-Property-Curves
- [33] (1987). Ohio Supercomputer Center. [Online]. Available: http://osc.edu/ark:/19495/f5s1ph73